AIAA JOURNAL
Vol. 48, No. 9, September 2010

# Toward Numerical Simulation of Fan Broadband Noise Aft Radiation from Aeroengines

G. Reboul* and C. Polacsek†
*ONERA, 92322 Châtillon Cedex, France*

DOI: 10.2514/1.J050237

**A first attempt to numerically simulate broadband noise transmitted through and radiated from a turbofan bypass duct is presented in this paper. Turbulent source assessment on the fan rows is left out here, and a generic power spectral density of in-duct acoustic pressure is imposed as an input to a computational aeroacoustic simulation performed using a time-domain Euler solver. The acoustic field is expanded over Fourier–Bessel modes, and the broadband noise behavior is modeled by introducing a random phase and by performing a quadratic averaging over independent runs. This broadband source generation approach is first validated in a semi-infinite annular duct by comparison with analytical solutions. The exhaust radiation problem from an idealized nozzle is then validated (for a single mode) by comparison to a Wiener–Hopf solution. In a second step, refraction effect through the shear layer is investigated for broadband noise. Computed results appear to be stable even in the presence of vorticity waves created in the shear layer. Then, the computation method is applied to a realistic nozzle. The only problem arising is the computational cost resulting in a limitation of high-frequency range limited here to 2–3 kHz (with around 600 propagating modes). Computed far-field directivities relative to idealized or realistic nozzle with similar input conditions are found to be rather close up to 90° of radiation angle.**

## Nomenclature

| | | |
|---|---|---|
| $A_{mn}(f)$ | = | amplitude of mode $(m, n)$ |
| $C_{mn}(R, f)$ | = | duct eigenfunction |
| $C_0$ | = | speed of sound |
| $(D, \theta, \varphi)$ | = | spherical coordinates |
| $\mathrm{d}p/\mathrm{d}n$ | = | pressure gradient normal to the integration surface |
| $E$ | = | ensemble average |
| $f$ | = | frequency |
| $K = \omega/C_0$ | = | wave number |
| $K_x$ | = | axial wave number |
| $M_i$ | = | jet Mach number |
| $M_o$ | = | ambient Mach number of uniform mean flow |
| $m_{\max}$ | = | maximum angular propagating mode order |
| $N_k$ | = | number of realizations |
| $N_{\mathrm{mod}}(f)$ | = | number of propagating mode |
| $n_{\max}$ | = | maximum radial propagating mode order |
| $p$ | = | pressure disturbance (acoustic in the linear domain) |
| $(R, \theta, X)$ | = | cylindrical coordinates |
| $R_{\mathrm{obs}}$ | = | radial position of the observer in far field |
| $R_s$ | = | radial position of the source |
| $S(f)$ | = | prescribed power spectral density |
| $S_{\mathrm{pp}}(f, R, \theta, X)$ | = | estimated power spectral density |
| $U_i = M_i C_0$ | = | jet velocity |
| $U_o = M_o C_0$ | = | ambient velocity |
| $V_n$ | = | velocity disturbance normal to the integration surface |
| $\theta_m$ | = | shear layer momentum thickness |
| $\varphi^k_{mn}$ | = | random phase |
| $\omega$ | = | angular frequency |

*Subscripts*

| | | |
|---|---|---|
| $m$ | = | angular mode order |
| $n$ | = | radial mode order |

*Superscript*

| | | |
|---|---|---|
| $k$ | = | realization number |

Presented as Paper 2009-3337 at the 15th AIAA/CEAS Aeroacoustics Conference (30th AIAA Aeroacoustics Conference), Miami, FL, 11–13 May 2009; received 22 September 2009; revision received 12 April 2010; accepted for publication 3 June 2010. 

*Ph.D. Student, Computational Fluid Dynamics and Aeroacoustics Department, 29 Avenue de la Division Leclerc, BP 72.

†Research Scientist, Computational Fluid Dynamics and Aeroacoustics Department, 29 Avenue de la Division Leclerc, BP 72.

## I. Introduction

SINCE fan broadband noise is becoming a major source of annoyance in modern aeroengines, prediction of this component is nowadays an important industrial need and probably one of the most challenging issues in turbomachinery aeroacoustics.

Several mechanisms are involved in the generation of fan broadband noise, but turbulence ingestion (rotor noise, fore radiation) and turbulent wake interaction (stator noise, aft radiation) are generally assumed to be dominant. This study focuses on the second. The main difficulty is the noise prediction at the source as studied in recent papers by means of computational methods [1–3] or analytical models [4,5]. However, acoustic radiation of fan broadband noise taking into account realistic geometries and refraction effects through the shear layer (exhaust case) should also be investigated. Moreover, although advanced developments based on Wiener–Hopf technique have recently been able to provide analytical expressions valid for the exhaust problem, these exact reference solutions are still limited to idealized plug flows [6,7].

The purpose here is to try to simulate broadband noise transmitted through and radiated from a realistic turbofan bypass duct using computational aeroacoustics (CAA). Nevertheless, direct source-to-far-field simulations are out of reach from full numerical approaches. The most practical way is to use a hybrid method aiming at splitting the overall problem in two specific parts devoted to source generation [computational fluid dynamics (CFD) and analytical model] and propagation/radiation through the inlet or exhaust (CAA). Current CAA investigations are mostly restricted to tonal noise [8–11], and the present study is dedicated to the extension to broadband noise.

The methodology discussed in the paper is sketched in Fig. 1. As a starting point, a source model for source generation (as discussed above) or an experimental database is assumed to provide the power spectral density (PSD) of the in-duct acoustic pressure field in the vicinity of the rows (bypass duct, downstream the stator in our case). For simplicity, a generic PSD is defined here and expanded over

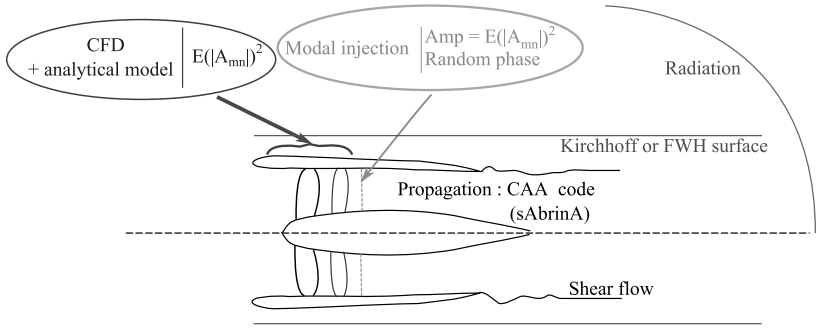


**Fig. 1 Schematic view of the methodology.**

Fourier–Bessel mode amplitudes of equal energy, denoted $E(|A_{mn}|^2)$, associated to each cut-on mode of angular order, $m$, and radial order, $n$. These modes are then injected with a random phase in a cross-section (source plane) as a boundary condition of a CAA Euler code. An ensemble average over a few independent runs (with various random phase sequences) is then performed in order to fit the noncoherent mode behavior of the broadband noise. The near-field CAA solution is extrapolated up to the far field by means of a classical Kirchhoff [10] or a Ffowcs Williams and Hawkings (FWH) integral [12], both written here in the frequency domain for convenience. CAA is performed using ONERA code *sAbrinA* [13], solving the full (nonlinearized) Euler equations applied to the perturbations. This code has already been intensively used for turbomachinery applications [10,14,15].

The paper is organized as follows: In Sec. II, the generation of broadband noise source is first discussed through a fully analytical approach describing the sound propagation in a semi-infinite annular duct with uniform mean flow. In particular, the convergence of results as a function of the number of realizations is investigated. Then, the numerical implementation and validation of the method is performed on the same case using *sAbrinA*. In Sec. III, the aft radiation from a finite annular duct with an infinite center body and considering two parallel (inside/outside) mean flows is treated. Gabard and Astley [7] have derived an exact analytical solution for this configuration and have proposed this idealized case as a benchmark for CAA [16]. This benchmark is clearly validated for a single mode, and the simulations are extended to broadband noise (multifrequency, multimode) to study the refraction effects on near- and far-field solutions due to the axial shear flow. A special care is taken when instability waves are created in the shear layer. Finally, Sec. IV is devoted to a preliminary application to a realistic double stream nozzle, for which mean flow is provided by a Reynolds-averaged Navier–Stokes (RANS) simulation. Capabilities and limitations of this numerical approach are then discussed.

## II. Broadband Noise Source Generation

### A. Broadbandlike Source Generation and Analytical Validation

One difficulty when trying to generate broadband noise in a CAA code using harmonic sources (modal approach) is to deal with the nondeterministic behavior of the turbulent source. Indeed, if several modes are generated at the same time, the contribution of each mode is added in a coherent way in the numerical process. All the more as solution of a time-domain Euler code with harmonic sources is obviously periodic. Practically, the broadband spectrum is estimated by performing a sampling over selected frequency bands. A simple way to achieve the incoherent mode behavior would be to run one computation per mode and to add each simulation result in an incoherent way afterward [17]. This is done when using analytical models, but the problem appears not to be manageable for numerical simulations if several hundreds of modes have to be considered. The approach proposed in this paper is to associate a random phase to each acoustic mode, and to launch independent simulations using different random phase sequences, the mode amplitude being set from a prescribed in-duct PSD of pressure. Note that a similar approach has been used to generate incoherent modes on a single frequency [18], and to simulate an isotropic turbulence [19]. Moreover, in appendix of their publication, Lafronza et al. [20] compare the two approaches (incoherent summation and random phase) in the case of sound attenuation by liners. This comparison leads to few discrepancies between the two methods.

This section is devoted to the validation of this methodology using theoretical form of the sound field in a semi-infinite annular duct with a uniform mean flow. We consider a generic PSD, $S(f)$ defined by

$$S(f) = \frac{1}{1 + (f/f_0)^{\gamma}} \tag{1}$$

$f_0$ and $\gamma$ are set to 1500 Hz and 2, respectively, in order to roughly fit the behavior of a fan broadband noise spectrum. $S(f)$ is plotted in thick line in Fig. 2a. This PSD represents the reference solution, assuming incoherent modes, so that the in-duct root mean square (RMS) pressure field is consequently constant in the axial and angular directions (as discussed later). Assuming an equal energy modal distribution, the PSD of the mode amplitude, $E(|A_{mn}(f)|^2)$ in $\mathrm{Pa}^2/\mathrm{Hz}$, is directly related to the number of cut-on modes $N_{\mathrm{mod}}(f)$ as

$$E(|A_{mn}(f)|^2) = \frac{S(f)}{N_{\mathrm{mod}}(f) C_{mn}(R_s, f)^2} \tag{2}$$

In Eq. (2), $R_s$ is the radial position of the source, $C_{mn}(R_s, f)$ is the duct eigenfunction. In the following sections, $R_s$ is set equal to the outer radius of the duct. We start here from the PSD of the acoustic pressure at the outer wall because such data can be practically obtained from standard measurement contrary to the PSD of the mode amplitude. Nevertheless, the majority of analytical models could provide $E(|A_{mn}(f)|^2)$ so that the modal input could be used directly without any assumption on modal energy distribution.

A single-realization mode amplitude (complex value), $A^k_{mn}(f)$, is computed by using a random phase uniformly distributed between 0 and $2\pi$, $\phi^k_{mn}$ with $k = 1 \ldots N_k$, $N_k$ being the number of simulations. It can be expressed as

$$A^k_{mn}(f) = \sqrt{E(|A_{mn}(f)|^2)}\, e^{i\phi^k_{mn}} \tag{3}$$

The analytical expression of in-duct acoustic pressure field then writes

$$P^k(f, R, \theta, X) = \sum_m \sum_n A^k_{mn}(f) C_{mn}(R, f) e^{i(K_x(f)X + m\theta)} \tag{4}$$

where $R, \theta, X$ are observer cylindrical coordinates, and $K_x$ is the axial wave number. For clarity, $S(f)$ is supposed to be defined using a frequency spacing of 1 Hz, so that $P^k$ is expressed in Pa.

Finally, an ensemble average over the $N_k$ realizations gives an estimation of the PSD of acoustic pressure, $S_{\mathrm{pp}}$:

$$S_{\mathrm{pp}}(f, R, \theta, X) = \frac{1}{N_k} \sum_{k=1}^{N_k} |P^k(f, R, \theta, X)|^2 \tag{5}$$

The validation case is a semi-infinite duct with an inner radius of 0.75 m, an outer radius of 1 m, and a mean (axial) Mach number equal to 0.45. The analysis is performed on six frequencies from 500 to

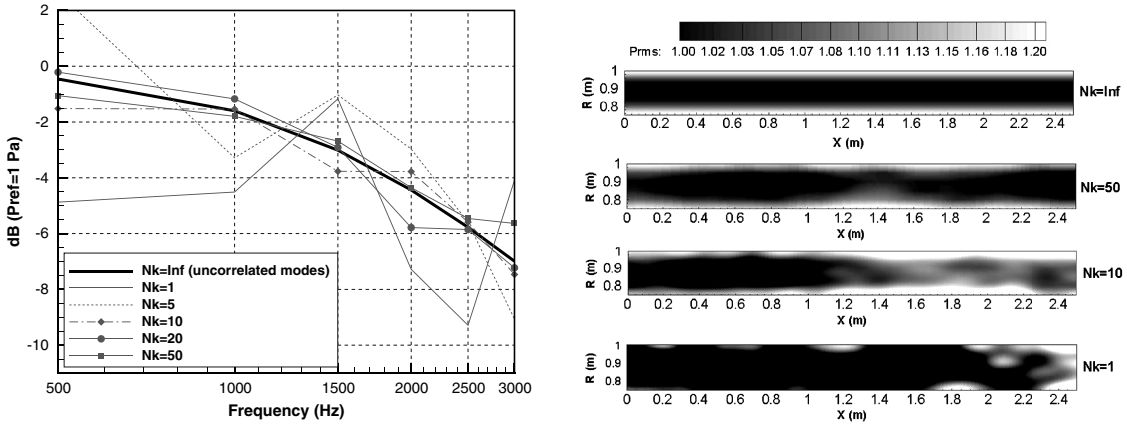


**a) Pressure PSD at outer wall** **b) In-duct RMS sound pressure ($Pa$)**

**Fig. 2 In-duct PSD estimation by averaging over $N_k$ realizations.**

3 kHz, and including all cut-on modes. 635 modes are cut-on at the maximum frequency. Figure 2a presents the pressure PSD at outer wall (at $X = 0.5$ m) for various values of $N_k$. $N_k = \text{inf}$ (infinity) is the reference solution obtained by adding the modes in a incoherent way. As expected, the convergence of the solution increases with $N_k$. Large statistical errors up to 5 dB are found for $N_k = 1$, and errors become acceptable for $N_k = 10$. A very good convergence is achieved for $N_k = 50$. Figure 2b displays the RMS values of acoustic pressure ($p_{\text{rms}}$) in an axial duct section, highlighting the axial dependency of the estimated fields compared with the constant reference solution ($N_k = \text{inf}$). The same tendency with respect to the number of realizations is observed, the case $N_k = 50$ giving the best accuracy.

As the phase term is a random variable, the variability between $S(f)$ and $S_{\text{pp}}(f)$ as a function of $N_k$ can be addressed, as done in Fig. 3.

The convergence trend appears to fit the conventional $1/\sqrt{(N_k)}$ law. This result provides a good validation of the proposed approach. Note that the error is almost independent of the frequency and consequently of the number of cut-on modes.

To summarize, in this test case for which more than 600 modes are cut-on, the present method allows us to reach a quite good accuracy by less than 50 runs instead of more than 600 (if incoherent sum of each mode contribution was made). However, with the prospect of industrial application, 50 is still a bit too high, and 10 appears more manageable (as considered in the following sections), even if error is still relatively high (about 30%). This is of course not an exact method but, on the other hand, is real broadband contribution perfectly incoherent? Another drawback of such harmonic source approach is that time correlation cannot be achieved since phase information is lost, so that only quadratic values in the frequency domain can be investigated.

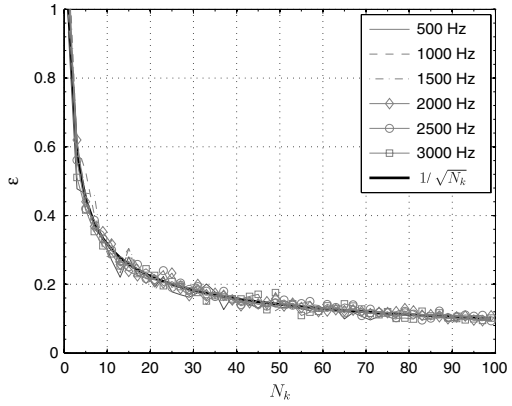


**Fig. 3 Statistical error between generic and regenerated spectrum.**

### B. CAA Implementation and Numerical Validation

The methodology described above is numerically applied using ONERA CAA code *sAbrinA*. This code solves the nonlinear Euler equations in perturbation form, with a sixth-order accurate finite-difference centered scheme in space, and a compact third-order Runge–Kutta algorithm for time marching. A tenth-order accurate symmetrical linear filter is applied to the flow variables at each time step to prevent occurrence of spurious wiggles. The code features multidimensional/multiblock structured grids. A slip condition is enforced at the solid body surface. To prevent numerical reflections from the boundaries of the computational domain, a high stretching is applied to the last 30 cells of the grid.

Two ways for generating Fourier–Bessel modes are available in *sAbrinA*. The first one uses an equivalent-source model [10,21] from which the modes are entered by means of suited distributed monopoles defined as source terms. The second option allows to inject these modes in terms of usual BC (boundary condition). It consists in imposing the downstream analytical solution [Eq. (4)] in fictitious cells at each time step, and taking into account the phase dependency. The equivalent-source model has the advantage to properly manage the duct end reflection, whereas it is not fully achieved on a usual BC [21]. In the BC approach, there is no damping zone upstream the injection plane and incoming waves amplitudes are imposed to zero. This abrupt transition may generate numerical reflections. However, the inverse method process used in the equivalent-source model is responsible for numerical errors that become nonnegligible when too many modes are involved as here. In the present case, it is important to have an accurate numerical description of the acoustic field since a great number of modes are generated, and the use of a BC mode injection appears to be more suited regarding this point. Consequently, possible standing waves due to numerical reflection from the injection plane are partly reduced by removing the acoustic modes close to the cut-off frequency (known to mostly contribute to these standing waves because of their large axial wavelength).

The case of the semi-infinite annular duct is considered again with the same generic spectrum, flow conditions, and geometry as in Sec. II.A. As a criterion, the largest wavelength computed is 5 m, which concerns only a few modes. With this limitation, 506 modes are propagating (instead of 635) with $m_{\max} = 51$ and $n_{\max} = 5$, respectively, for the highest angular and radial mode orders. The computation is fully tridimensional since more than one mode are propagating, and one cannot take advantage of the axisymmetry of the mode, neither using recently developed 2.5D formulation [22] nor a three-dimensional computation per sector (periodical azimuthal boundary condition). The methodology is performed by averaging over 10 runs ($N_k = 10$) and numerical predictions are compared with the theory in Fig. 4.

Figures 4a and 4b respectively show the PSD of pressure at outer wall and the RMS levels along a duct section. Theoretical and numerical predictions in Fig. 4a match fairly well excepted a slight deviation of 0.4 dB at the highest frequency (3 kHz). In-duct RMS

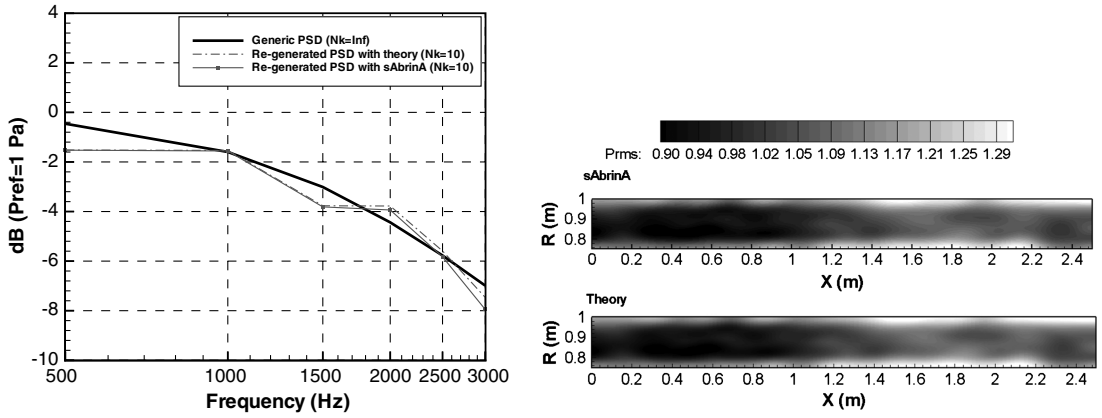


**a) Pressure PSD at outer wall** **b) In-duct RMS sound pressure (*Pa*)**

**Fig. 4 Numerical and theoretical PSD estimated by averaging over 10 realizations.**

pressure fields in Fig. 4b are almost identical. These results confirm the ability of *sAbrinA* to simulate properly a broadbandlike source propagation, starting from a generic prescribed PSD. This also confirms that the numerical simulations have a fully coherent mode behavior and that the convergence law pointed out theoretically in Sec. II.A can be reached numerically.

## III. Idealized Duct Radiation in a Parallel Shear Mean Flow

### A. Monomode Validation

One of the main goals of this paper is to study the effect of a shear mean flow on the radiation of fan broadband noise (exhaust radiation). Before discussing the broadband noise issue, a monomode validation on an idealized configuration is done. Gabard and Astley [7] derived an exact analytical solution for sound radiation from a semi-infinite unflanged annular duct with an infinite center body using a Wiener–Hopf technique. The duct carries a jet (uniform) which issues into a uniform external flow. The model also takes into account the instability waves created in the shear layer. This case provides an idealized representation of a turbofan exhaust. Gabard et al. [16] defined a configuration to be used as a benchmark for CAA. This benchmark has already been studied by Casalino and Genito [23].

Figure 5 describes the configuration with a sketch of the geometry (Fig. 5a) and a partial view of the CAA grid showing the computation domain (Fig. 5b). The stretching of the grid is clearly visible. Among the different validation cases, a single mode (17, 2) at reduced frequency $KR = 30$ has been chosen. The jet Mach number ($M_i$) is set to 0.45 and the outer Mach number ($M_o$) to 0.25. The annular duct remains the same as in Secs. II.A and II.B. For comparison, the uniform mean flow case ($M_i = M_o = 0.45$) is also addressed. Even if only one mode is generated, a three-dimensional computation is performed with the prospect of a multimode simulation. Hence, the mesh reaches 9 million nodes with a points per wavelength (PPW) condition ensuring that at least 10 points are covering the smallest wavelength (PPW $\times \Delta x = \frac{C_0/f}{1+M_{\max}}$, $M_{\max}$ being the highest Mach number, $\Delta x$, the mesh size, and $C_0$, the speed of sound). One hundred eighty planes are used in the azimuthal direction, and the radial and longitudinal grid spacings are set equal.

The near-field solution (Fig. 6) does not exhibit any instability wave in the shear layer contrary to the theory [7] and to some simulations using linearized Euler equations [24]. Indeed, beyond a sharp trailing edge, the Kutta condition forces the pressure jump to be zero, but acoustic waves passing the edge induce an oscillatory nonzero velocity at the edge. To maintain the Kutta condition, a vorticity wave is created. For an incompressible, isothermal, parallel shear layer between a jet and a fluid at rest, Michalke [25] indicates that the stability is ensured when

$$\frac{\omega\theta_m}{U_i} > 0.25 \tag{6}$$

$\omega$ is the angular frequency of the incoming acoustic wave, $\theta_m$ is the momentum thickness of the shear layer, and $U_i$ is the jet velocity. In the present case, $\theta_m$ is zero (in a numerical point of view, the transition occurs over a mesh size) and the condition should never be satisfied. The generation of instabilities is indeed closely related to the discretization in the radial direction. The finer the mesh is, the more the numerical model tends toward a zero thickness shear layer. Consequently, the finer the mesh is, the higher is the frequency limit for the generation of instabilities. Thus, in the benchmark case, the mesh is fine enough to support acoustic waves at 1624 Hz and coarse enough (in the radial direction) not to create instabilities.

The far-field directivities are obtained by coupling the near-field acoustics to a conventional Kirchhoff integral [10]. Following Casalino and Genito [23], the Kirchhoff surface is a cylinder surrounding the nozzle (see Fig. 5b), with an axial extent covering the entire computation domain. The surface is not closed at the ends in order to prevent from violating the uniform flow assumption. However, since the mean flow is uniform right after the (thin) shear layer, the cylinder can be placed very close to the nozzle ($R$= 1.1 m), so that main sources are expected to be captured.

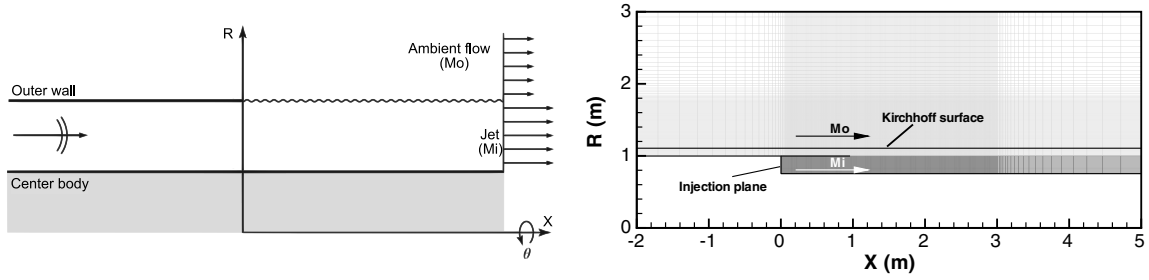


**a) Sketch of the idealized nozzle** **b) Partial view of CAA grid**

**Fig. 5 Idealized nozzle case.**

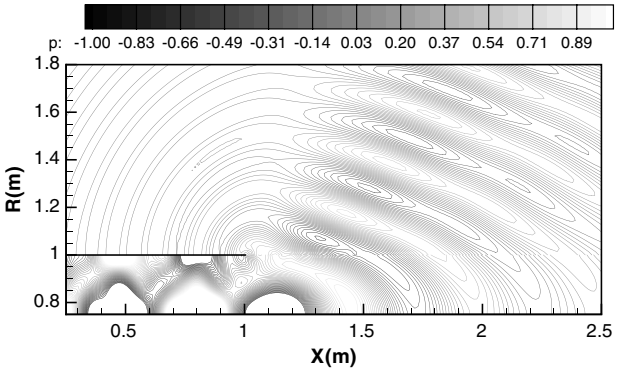


**Fig. 6 Simulated disturbance pressure field, Pa.**

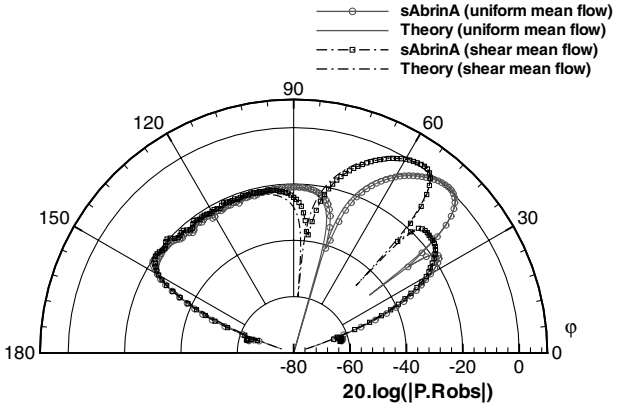


**Fig. 7 Validation of far-field directivities: simulations versus exact Wiener–Hopf solutions of Gabard and Astley [7].**

Figure 7 presents the far-field pressure directivities obtained numerically (*sAbrinA*/Kirchhoff) and analytically (Gabard and Astley), for observers located in far field ($R_{\text{obs}} = 100$ m from the center of the duct exit plane). A good agreement is found for both uniform and parallel shear mean flow conditions. One can note the good dynamic range (about 60 dB) of the numerical predictions in the extinction areas as well as for high and low radiation angles.

### B. Broadband Noise Radiation

The computation presented in Sec. III.A is extended to broadband noise radiation, considering once again the uniform and nonuniform mean flow conditions. As previously said, one of the main limitations of the technique is that the computation has to be three-dimensional, and is consequently very expensive in CPU time and memory size. For this reason, the input PSD (the same as used in Sec. II.B) is limited to 2500 Hz with $m_{\max} \leq 40$. However, the modes are numerous enough (310) to considered the source as broadband and to demonstrate the advantage of the present method. A 12 million node mesh is designed, with PPW = 9, and the time step is such that maximum Courant–Friedrich–Lewy (CFL) number is equal to 0.58

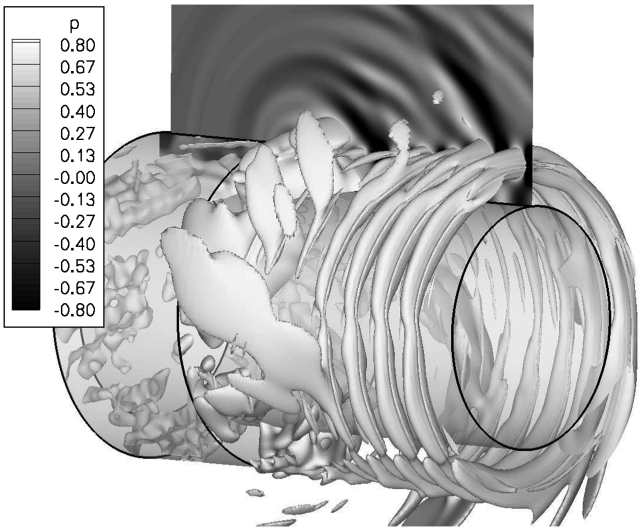


**Fig. 9 Vorticity waves visualization (isovalue of pressure at 0.7 Pa).**

to ensure a good stability. The computation duration required to reach a statistically converged solution is about 25 times the longest acoustic period, and the CPU time is approximately 20 hours on a NEC-SX8.

#### 1. *Near-Field Analysis on a Coherent Mode Simulation*

As mentioned before, the present method is not suited to perform time-domain analyses. Nevertheless, it can be interesting to analyze the temporal behavior relative to a single realization (that is to say a coherent mode simulation). Figures 8a and 8b present the near-field pressure perturbation field obtained without and with shear mean flow.

Contrary to the single mode result in the previous section, the simulation with parallel shear flow reveals an instability mode. However, these vorticity waves are clearly less intense than in the theoretical results of Gabard and Astley [7] or in the numerical simulations of Kok [24], and the conical front shape is not so highlighted. In his study, Kok [24] said that the computation may break down before convergence because of the growing of the unstable mode both in space and time. In our case, simulations can reach a statistically converged state even in the presence of such instabilities. Differences could be probably attributed to nonlinear effects that are included in our full Euler computations as discussed by Bailly and Juvé [26]. However, for shear layers with higher gradient, numerical divergence may occur. To improve the stability, a drastic reduction of the CFL number or an artificial increase of the shear layer momentum thickness [24] can be applied.

In Fig. 9, isovalue (0.7 Pa) of pressure perturbation is plotted simultaneously with the contour map of the pressure perturbation in a plane. This representation is helpful to visualize the vorticity waves shape, and one can remark the nonperfect axisymmetry of the instability mode.

A complementary analysis has also been performed in order to check the convection speed of the acoustic and vorticity modes

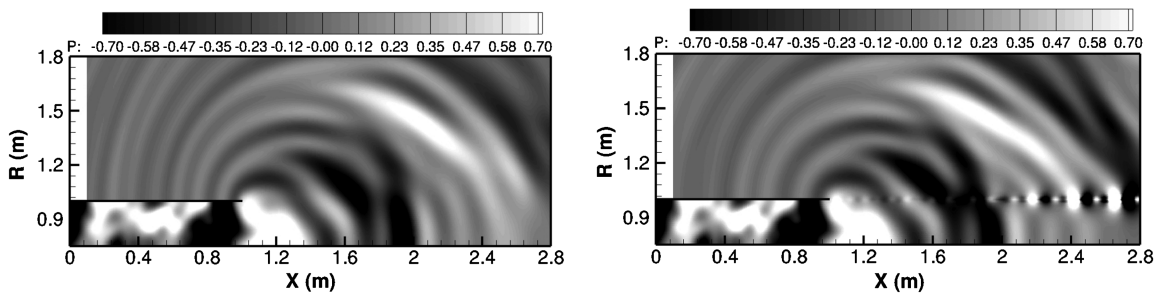


**a) Uniform mean flow** **b) Non-uniform mean flow**

**Fig. 8 Simulated pressure disturbance fields, Pa relative to a single run.**

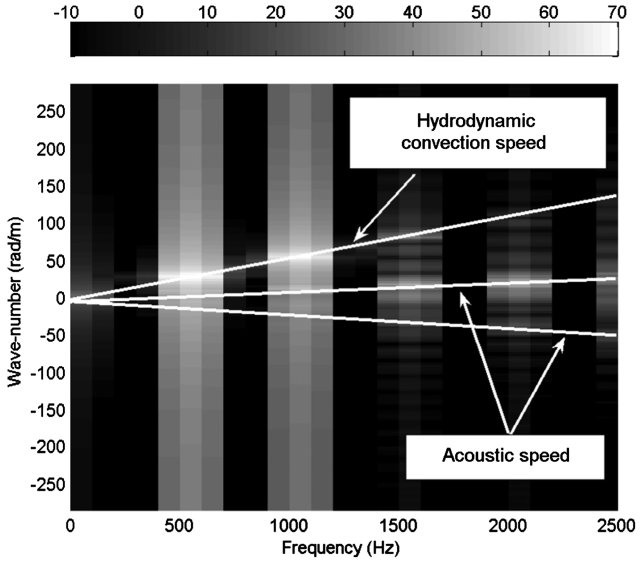


**Fig. 10 Wave number/frequency spectrum, dB.**

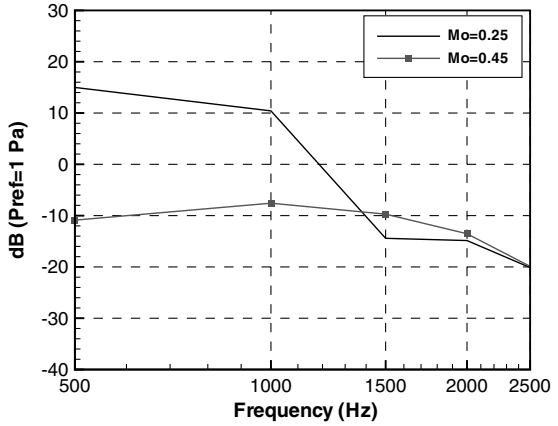


**Fig. 11 PSD of pressure in the shear layer ($X = 2.5$ m, $R = 1$ m).**

displaying a spectrum in the wave number/frequency domain (Fig. 10). The analysis is made on a mesh line located at $R = 1$ m from $X = 0.1$ to 2.8 m. As the spectrum is sampled using only five discrete frequencies, convection information is highlighted by discrete spots at each corresponding frequency. The spots are linked using over-plotted white lines, the slopes of which give an estimate of the convection speed. The two acoustic speeds (upstream and downstream, i.e., $C_0 \pm U_0$) are clearly addressed. The convection speed of the vorticity modes is also revealed and found to be equal to 118.3 m/s. This value is consistent with convection speed in a shear layer, known to be $(U_0 + U_i)/2$, i.e. 119 m/s in our case.

The graph in Fig. 10 shows that spots at 500 and 1000 Hz for the instability waves are more intense than spots at higher frequencies. These observations are confirmed in Fig. 11, showing the PSD of

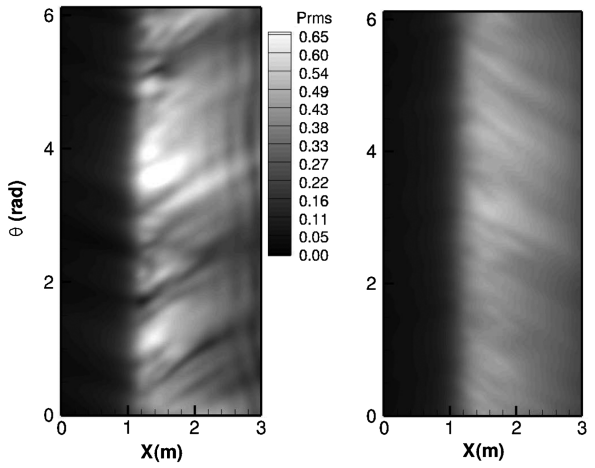


**a) Coherent** **b) Incoherent**

**Fig. 13 RMS pressure fields, Pa, on a cylindrical surface using a) coherent and b) incoherent computations.**

pressure on the mean flow separation line (with and without shear flow). PSD in the presence of unstable modes is 25 dB higher than without vorticity at 500 Hz, 18 dB higher at 1000 Hz, and levels tend to convergence at higher frequencies. These results are in agreement with comments made in Sec. III.A. All the frequencies should theoretically be excited since the momentum thickness is zero [see Eq. (6)]. However, the shear layer thickness is artificially increased by the numerical model (grid spacing) so that only low frequency waves are responsible for the generation of instabilities.

*2. Near- and Far-Field Analysis on an Incoherent Mode Simulation*

The same simulations are performed by averaging over 10 independent runs. Again, it is important to say that we limit $N_k$ to 10 for practical reasons (CPU time), and that the accuracy of the PSD estimate could be improved by increasing this value. We are mainly focusing on reliable tendencies and applicability of the numerical approach.

RMS levels of pressure disturbance field obtained in the near-field are displayed in Figs. 12a and 12b for uniform and nonuniform mean flow, respectively. The averaging tends to emphasize the vorticity field, as seen in Fig. 12b, the instability waves being convected and spread out within a conical area.

A good criterion for convergence status in term of realization number is to check for axisymmetry. The next figure shows the RMS pressure field along an unrolled cylindrical surface ($R = 1.26$ m) using a coherent mode simulation (Fig. 13a), and after averaging over 10 simulations (Fig. 13b). As expected, the statistical averaging forces the pressure pattern to become roughly axisymmetrical, which of course has a significant impact on acoustic far-field predictions.

Once again, near-field results are extrapolated to the far field using an integral method. To study the effect of the vorticity field with respect to usual Kirchhoff method, a FWH formulation is also implemented for comparison. The FWH porous surface formulation is expected to be less sensitive to vortical waves. Both methods are compared with

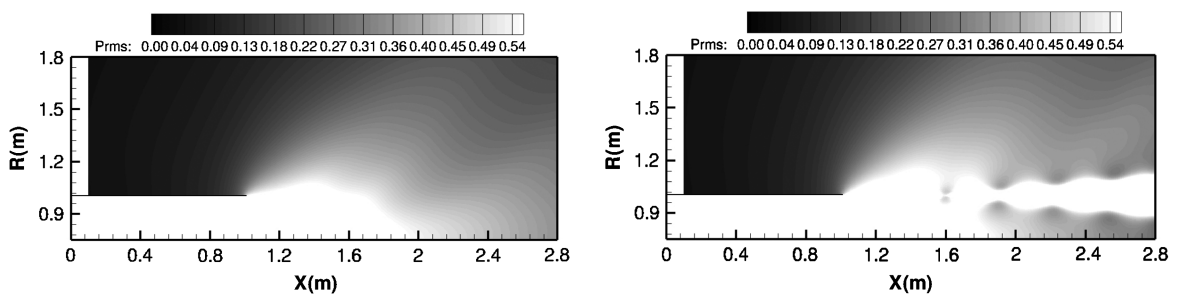


**a) Uniform mean flow** **b) Non-uniform mean flow**

**Fig. 12 Regenerated RMS contour levels of pressure disturbance field, Pa.**

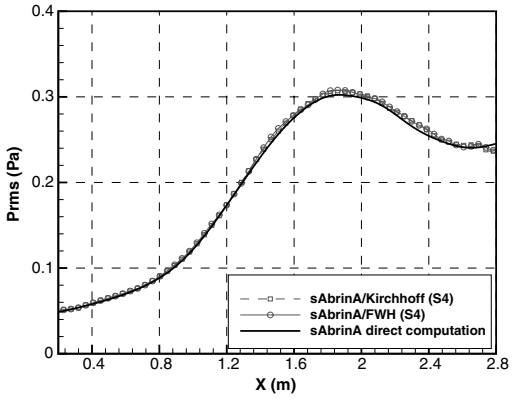


**Fig. 14 Comparison between direct CAA and Kirchhoff or FWH coupling on the uniform mean flow case (integration surface $S4$ at $R = 1.1$ m).**

the direct CAA solution. First, the uniform mean flow case is considered with a surface located at $R = 1.1$ m. Results are displayed in Fig. 14. No differences are observed between the two integral methods and the agreement with the direct computation is good.

For the shear mean flow case, different surface locations are investigated, close ($S4$ at $R = 1.1$ m) to far ($S1$ at $R = 1.33$ m) from duct axis. The surface $S4$ is very close to the shear layer and partly crosses the vorticity field, and the results show high oscillations, especially for the FWH formulation. The Kirchhoff method starts to provide good results with the surface $S3$ while the FWH result has larger discrepancies in the downstream part. Such results are surprising since the FWH method should be less sensitive to the location of the integration surface. For the two last surfaces ($S1$ and $S2$), the two methods give similar estimations, and the agreement with the direct computation is quite good.

To try to understand what is wrong in the use of the FWH formulation key field values related to main contributing source terms are displayed on the different unrolled integration surfaces. RMS levels of velocity component normal to the surface ($V_n$) and RMS levels of pressure are displayed in Figs. 15a and 15b. The RMS levels of pressure gradient normal to the surface ($\mathrm{d}p/\mathrm{d}n$) are shown in Fig. 15c.

The analysis being limited to a single realization, the contour maps reveal strong three-dimensional effects that should be greatly smoothed by the averaging process (as discussed previously). Anyway, intense sources (white spots) distributed along a strip at the downstream boundary of the integration surface are clearly seen on all fields ($V_n$, $p$, $\mathrm{d}p/\mathrm{d}n$) for the closest surfaces ($S4$ and $S3$). These spurious sources are the prints of the vortical waves, having intense levels at these locations which particularly impact the normal velocity field (source term in the FWH formulation not present in the Kirchhoff integral). The truncation of these sources in the integration process is probably responsible for the oscillations observed in

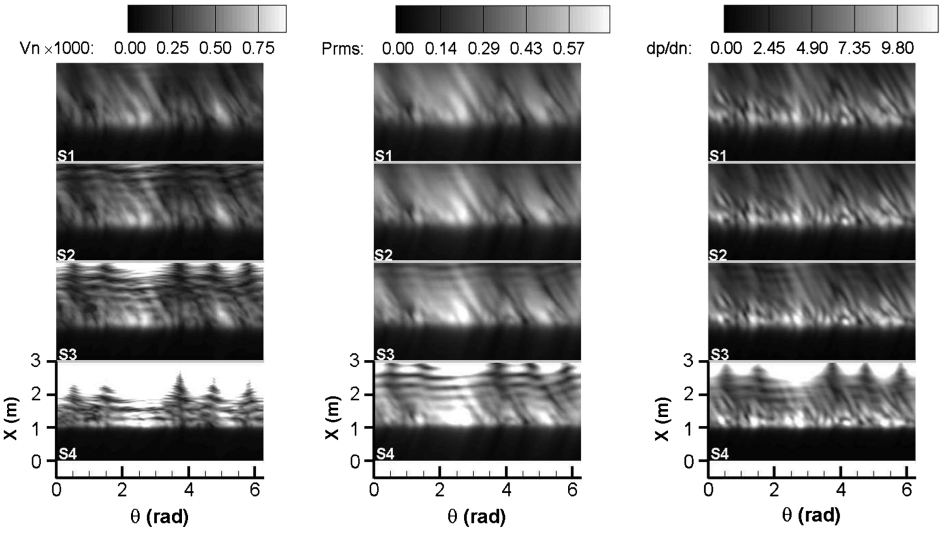


**a) $V_n$ RMS levels (m/s)** **b) $p_{rms}$ levels (Pa)** **c) *dp/dn* RMS levels (Pa/m)**

**Fig. 15 Comparison between direct CAA and Kirchhoff or FWH coupling on the nonuniform mean flow case.**

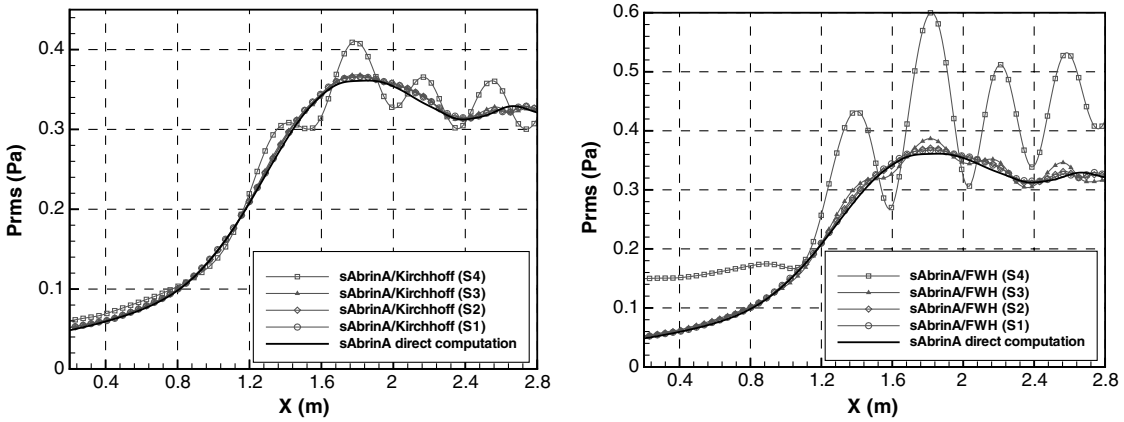


**a) Kirchhoff integral** **b) FWH integral**

**Fig. 16 Effect of integration surface position on $V_n$, $p$ and $\mathrm{d}p/\mathrm{d}n$ RMS levels.**

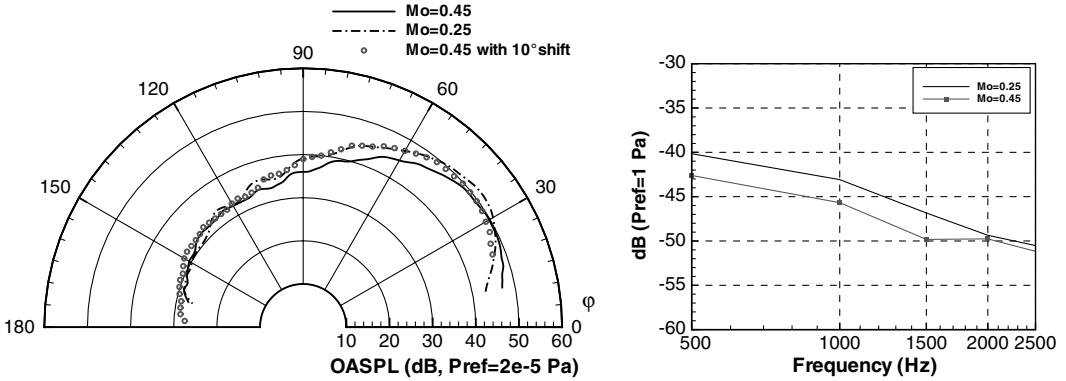


a) Far-field directivity patterns b) Far-field PSD (45°)

**Fig. 17 Far-field results using a Kirchhoff integral.**

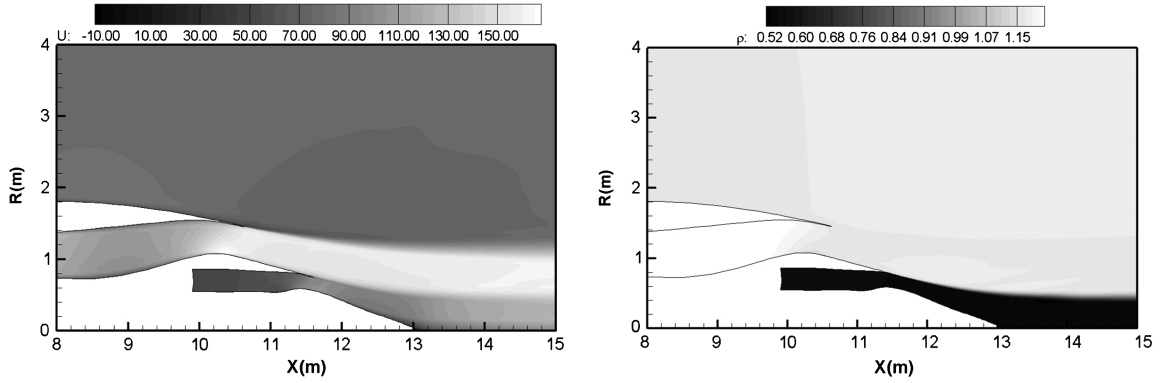


a) Axial velocity ($m.s^{-1}$) b) Density ($kg.m^{-3}$)

**Fig. 18 Mean flow characteristics (RANS computation from Airbus–France).**

Fig. 16. $\mathrm{d}p/\mathrm{d}n$ source term is known to have a major contribution in the Kirchhoff integral, and the $\mathrm{d}p/\mathrm{d}n$ contour maps show that sources vanish rapidly at the downstream boundary (from *S*3 location) whereas they are still present in the $V_n$ maps. Consequently, the truncation effects have a stronger impact on the FWH-based integration (see *S*3 and *S*4 results in Fig. 16b). A practical way to prevent from such oscillations would be to use a conical surface integration (as done in jet studies [27]) following the spreading of the instability waves. Nevertheless, for the present benchmark using cylindrical surface integration, the conventional Kirchhoff formulation appears better suited. It will be adopted for the continuation of the study.

Far-field overall sound pressure level (OASPL) calculated for an observer located at 100 m from the duct exit is presented in Fig. 17a, as well as the pressure PSD at radiation angle of 45° in Fig. 17b, for the two flow conditions. These results are obtained using the Kirchhoff method with the surface *S*3. The directivity patterns reveal a wide lobe characteristic of turbofan broadband noise radiation. Note that the first 10° and the last 10° have been removed since integration surface is not closed, and results are not relevant for such positions. The main difference between uniform and nonuniform flow solutions is an angular shift of approximately 10° as clearly shown in Fig. 17a (dashed curve) corresponding to the uniform flow directivity result shifted by 10°. A slight increase of the maximum (approximately 2 dB) is found in the nonuniform flow (compare 30 and 40°). Another important point is that there is not a strong increase of PSD level at low frequency (Fig. 17b) as observed in near field (Fig. 11). These results confirm that the vorticity waves should have a weak contribution to the far-field radiation.

## IV. Realistic Nozzle Case

A first application of our numerical procedure to a realistic nozzle with a primary and secondary shear mean flow provided by a RANS computation is proposed in this section. In addition to showing that the method can be applied to a complex configuration, another goal is also to compare the broadband noise propagation/radiation simulation between a realistic geometry and the idealized nozzle previously studied.

The geometry and flight conditions are issued from an Airbus-France/ONERA collaboration in the framework of AMBIANCE project [28]. The RANS solution has been provided by Airbus–France using ONERA code *elsA*, a second order accurate finite volume code. A certification point at approach conditions is considered. Figures 18a and 18b respectively show the mean axial velocity and the mean density field. The mean flow appears to be highly heterogeneous.

The main characteristics for inlet and far-field conditions are listed in Table 1 where $M$, $P$, $T$, $C_0$ and $\rho$ stand for the Mach number, the pressure, the temperature, the speed of sound, and the density, respectively.

Starting from the nozzle geometry, a new CAA axisymmetric grid (Fig. 19) has been designed in order to be more suited to acoustic propagation requirements and to the coupling with the Kirchhoff integral. The RANS mean flow solution is interpolated from the CFD to the CAA grid using the software TECPLOT. The three-dimensional CAA mesh is simply obtained by rotation in the azimuthal direction, leading to about 13,700,000 nodes over three blocks.

**Table 1 Main characteristics of in-flight aerodynamic conditions**

| Approach | $M$ | $P$, Pa | $T$, K | $C_0$, m.s$^{-1}$ | $\rho$, kg.m$^{-3}$ |
|---|---|---|---|---|---|
| Bypass duct | 0.319 | 107.718 | 306.1 | 350.694 | 1.22651 |
| Core duct | 0.114 | 103.646 | 664.75 | 516.880 | 0.543 |
| Infinite space | 0.222 | 99.940 | 297.4 | 345.71 | 1.1701 |

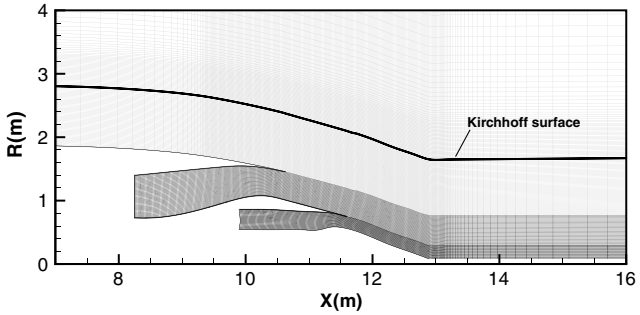


**Fig. 19 Section view of CAA three-dimensional multiblock grid.**

The main issue when using such structured mesh is the very small cell size near the axis. Since *sAbrinA* uses an explicit scheme, CFL must be lower than one and consequently the time step is trimmed by these smallest grid cells. To limit this value, a small domain encompassing the nozzle axis was removed. This should not perturb the simulation since sound level in this area is known to be low. Also, in order to reduce the CPU time, the prescribed pressure PSD frequency range is limited from 400 to 2000 Hz, with a frequency spacing equal to 400 Hz. However, the geometry being larger than in Secs. II and III, the corresponding $KR$ (based on outer radius in the injection plane) is relatively high ($KR = 54$ instead of 55 in the infinite duct case). A minimum PPW of eight is ensured (limitation for a satisfactory approximation of the derivative operator [29]), and maximun CFL number reaches an extreme value of 0.99. The simulation is conducted over 28 largest period to get a statistically converged solution, requiring 85 hours of CPU time on a NEC SX8. Concerning the modal content, 547 cut-on modes are generated by setting $m_{\max} = 40$ and $n_{\max} = 8$.

An idealized duct (as described in Sec. III) is designed to match as well as possible the realistic nozzle conditions. The inner and outer radii are equal to the radii of AMBIANCE nozzle at the injection plane as well as the aerodynamic characteristics (bypass duct in Table 1) in the jet area. The free stream conditions are those in the infinite space. The grid size and PPW are close to the realistic nozzle case, but due to the absence of primary stream, the time step is much larger and the simulation much faster.

### A. Near-Field Analysis

Here again, some preliminary temporal analyses on a single run (coherent mode simulation) are proposed. Pressure perturbation snapshots simulated for both configurations (idealized and realistic nozzle) are presented, respectively, in Figs. 20a and 20b at the same time step. Only the low frequency patterns are similar, whereas large discrepancies occur for higher frequencies due to geometrical changes. Instabilities are stronger in the realistic case, mainly due to an increase of the axial velocity through the (narrowed) bypass-duct exhaust. A view of the vorticity waves is proposed in Fig. 21 by plotting the isovalue contours of pressure perturbation.

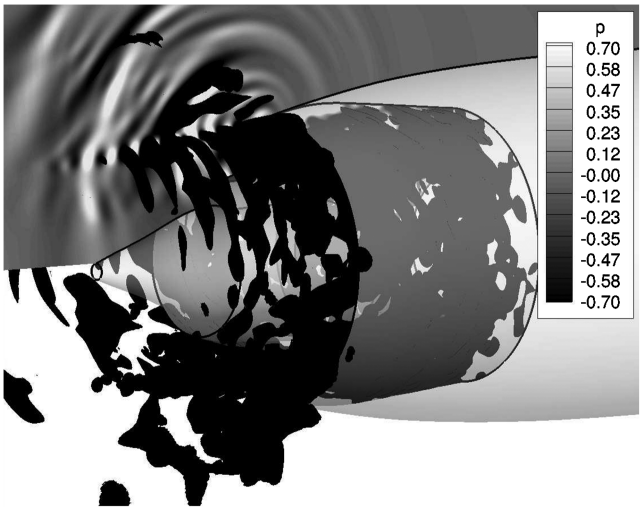


**Fig. 21 Vorticity waves visualization (isovalue of pressure at −0.7 Pa).**

The instabilities are found to be much less axisymmetric than in the idealized duct configuration, such that no vorticity is created for some azimuthal angles. Also, whereas the vorticity mode grows almost uniformly in the axial direction for the idealized duct configuration, the spreading (increase of the momentum thickness) of the realistic shear layer in the axial direction tends to damp the vorticity after some distance. This effect is clearly seen in Fig. 22b where the RMS levels obtained after averaging over 10 simulations are plotted. The agreement between the two solutions (Figs. 22a and 22b) is good in the upper region (beyond $R = 1.5$ m) where the low-level and high-level patterns are almost similar. On the other hand, in the vicinity of the center body, reflections on the infinite wall lead to an amplification of the level.

### B. Far-Field Results

Last analysis is devoted to far-field predictions using *sAbrinA*/Kirchhoff. Here too, different positions of the Kirchhoff surface have been tested due to the presence of high inhomogeneous mean flow, and for which uniform flow conditions are ensured at a larger distance compared with the idealized case (see Fig. 19). For the simplified nozzle, the same location as in Sec. III.B is used that is to say 0.18 m in the radial direction from the outer duct wall. Resulting far-field directivities and PSD are displayed in Fig. 23a and 23b respectively.

The directivity patterns are found to be rather close up to a radiation angle of 90°. Beyond, differences are noticeable and may be due to scattering effects that are quite sensitive to the shape of the lips and outer walls of the nozzles. One can note that PSD levels with a realistic shape are lower than with the idealized duct for lower frequency. As hub-to-tip ratio at exit plane of the realistic case is smaller than in the idealized case, the lower frequencies are probably

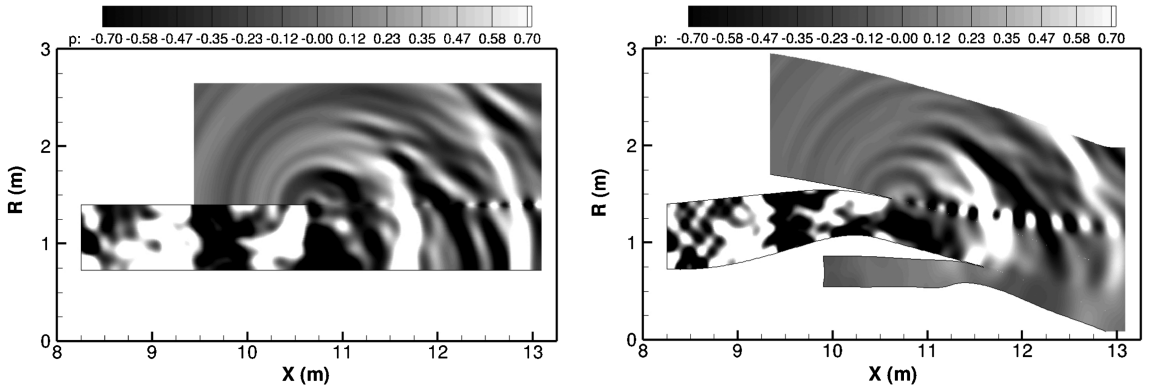


**a) Idealized nozzle** **b) Realistic nozzle**

**Fig. 20 Pressure perturbation fields, Pa.**

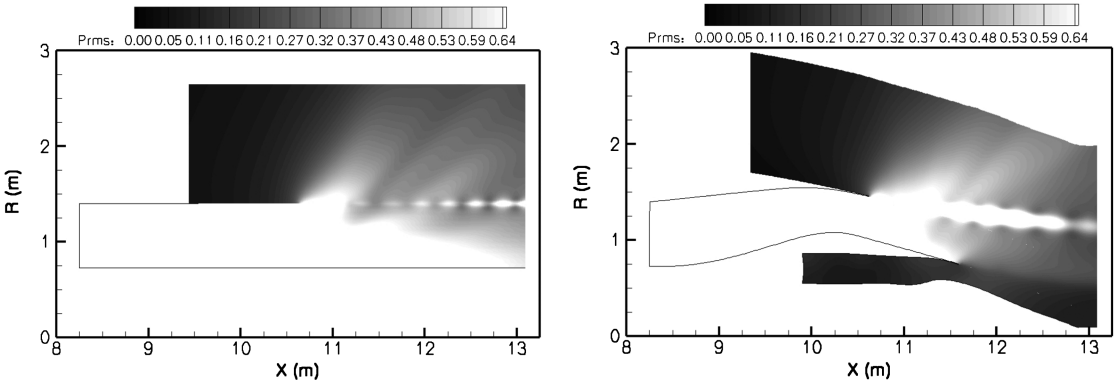


**a) Idealized nozzle** **b) Realistic nozzle**

**Fig. 22 Regenerated RMS levels, Pa.**

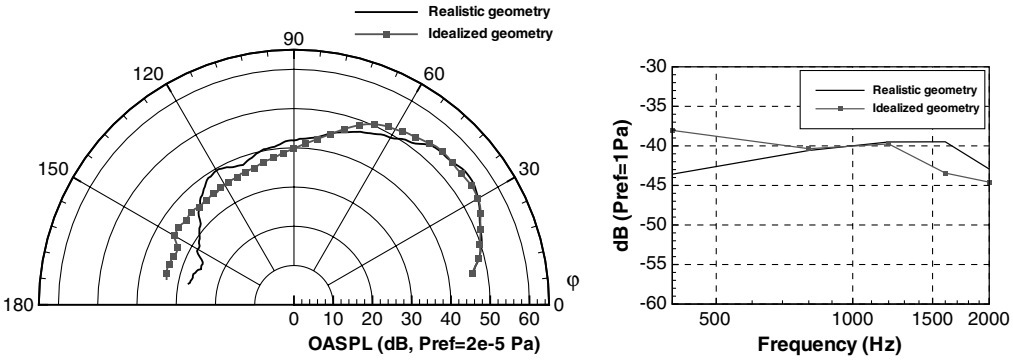


**a) Far-field directivity patterns** **b) Far-field pressure PSD(45 $^o$)**

**Fig. 23 Far-field predictions using *sAbrinA*/Kirchhoff.**

more reflected on the duct exit. On the other hand, for higher frequencies the inverse trend is observed so that finally, maximum OASPL in the arc 10–50° are almost equal. This tends to show that the idealized duct seems to be a reasonable approximation, and that semi-analytical solutions based on Wiener–Hopf techniques are still a good candidate for industrial applications, particularly for the design process.

Anyway, the numerical approach proposed here appears to be applicable for industrial cases thanks to the fact that simulations are fully independent and can be run simultaneously. Since the computations have to be three-dimensional, the CPU cost becomes very expensive as far as high-frequency predictions are needed. However, turbofan broadband noise spectrum is rather flat, and consequently a large frequency spacing of 400 or 500 Hz (as used in this paper) should be practically acceptable.

## V. Conclusions

In this paper, a first attempt to simulate broadband noise propagation and aft radiation from a turbofan engine using a numerical approach has been investigated. A methodology based on the injection of broadband sources in a CAA Euler code, by means of equally energy distributed Fourier–Bessel modes with random phases has been successfully applied to academic and more advanced configurations. Modal amplitudes are deduced from the sampling of a prescribed pressure spectrum, and the PSD is estimated by means of a quadratic averaging over a few independent runs (performed by setting different random phase sequences). This allows us to fit the incoherent mode behavior of fan broadband noise. A convergence trend with respect to the decrease of statistical errors follows a $1/\sqrt{(N_k)}$ law ($N_k$ being the number of simulations), so that reliable predictions can be achieved by using only 10 averages. The method has been used to study the aft radiation from an idealized duct case recently proposed as a CAA benchmark. As a first step, the CAA solution has been accurately validated for a single mode. Then, with only 10 simulations, the RMS pressure field was almost axisymmetric, and was characterized by a large directivity lobe (representative of fan broadband noise). A special care has also been taken on the effect of instability waves. Contrary to numerical divergences often observed when using linearized Euler equation codes, the nonlinear terms included here seem to improve the stability of the computation even when strong vorticity modes are created in the shear layer. However, by comparing uniform and nonuniform mean flow predictions, it seems that vorticity waves contribution to the acoustic far-field radiation is small, and so the main effect is due to the refraction that tends to deviate the directivity lobe from the duct axis. Finally, a realistic nozzle with a RANS mean flow solution in the primary and secondary ducts has been simulated and compared with the idealized case with source frequency from 400 to 2000 Hz. Even if near-field results reveal noticeable differences, mainly due to different duct exit ratio and center body shape, the far-field directivities follow the same trend up to 90° of radiation angle. This result tends to show that the idealized duct solution proposed by Gabard and Astley [7] is a good approximation, even if larger discrepancies occur for higher radiation angles. Vorticity modes are still present, but the natural spreading of the shear layer (compared with the nonphysical parallel shear flow) tends to damp the instabilities after some distance.

To summarize, the present method appears to be reliable for advanced configurations since runs are fully independent, and so can be run simultaneously. However, because the computations have to be fully tridimensional since a wide frequency range and numerous modes have to be included, the CPU cost is very expensive. The parallelization of the code (underway) is required in order to apply the methodology to industrial configurations [28].

## Acknowledgments

The authors acknowledge Y. Druon of Airbus–France for providing the AMBIANCE project data and G. Gabard for supplying

the analytical results on the aft radiation benchmark. S. Redonnet is also thanked for his major contribution to the development of the *sAbrinA* code.

## References

[1] Atassi, H. M., and Vinogradov, I. V., "Modelling Broadband Fan Noise and Comparison with Experiments," 13th AIAA/CEAS Aeroacoustics Conference, AIAA Paper No. 2007-3691, 2007.

[2] Reese, H., Kato, C., and Carolus, T., "Large Eddy Simulation of Acoustical Sources in a Low Pressure Axial-Flow Fan Encountering Highly Turbulent Inflow," *Journal of Fluids Engineering*, Vol. 129, No. 3, 2007, pp. 263–272. doi:10.1115/1.2427077

[3] Reboul, G., Polacsek, C., Lewy, S., and Heib, S., "Ducted-Fan Broadband Noise Simulations Using Unsteady or Averaged Data," *Inter-Noise 2008*, 2008.

[4] Nallasamy, M., and Envia, E., "Computation of Rotor Wake Turbulence Noise," *Journal of Sound and Vibration*, Vol. 282, Nos. 3–5, 2005, pp. 649–678. doi:10.1016/j.jsv.2004.03.062

[5] Posson, H., Moreau, S., and Roger, M., "Fan-OGV Broadband Noise Prediction Using a Cascade Response," AIAA Paper 2009-3150, 2009.

[6] Demir, A., and Rienstra, S., "Sound Radiation from an Annular Duct with Jet Flow and a Lined Centerbody," 12th AIAA/CEAS Aeroacoustics Conference, AIAA Paper 2006-2718, 2006.

[7] Gabard, G., and Astley, R., "Theoretical Model for Sound Radiation from Annular Jet Pipe: Far- and Near-Field Solutions," *Journal of Fluid Mechanics*, Vol. 549, 2006, pp. 315–341. doi:10.1017/S0022112005008037

[8] Zhang, X., Chen, X., Morfey, C., and Tester, B., "Computation of Fan Noise Radiation Through a Realistic Engine Exhaust Geometry with Flow," Ninth AIAA/CEAS Aeroacoustics Conference, AIAA Paper No. 2003-3267, 2003.

[9] Bréard, C., "Acoustic Propagation and Radiation Modeling of Lined Duct with Linear and Non-Linear Frequency-Domain Solver," Ninth AIAA/CEAS Aeroacoustics Conference, AIAA Paper No. 2003- 3265, 2003.

[10] Polacsek, C., Burguburu, S., Redonnet, S., and Terracol, M., "Numerical Simulation of Fan Interaction Noise Using a Hybrid Approach," *AIAA Journal*, Vol. 44, No. 6, 2006, pp. 1188–1196. doi:10.2514/1.10688

[11] Casalino, D., and Barbarino, M., "Turbofan Aft Noise Radiation : Progress Towards a Realistic CAA Simulation," 14th AIAA/CEAS Aeroacoustics Conference, AIAA Paper No. 2008-2882, 2008.

[12] Lockard, D. P., and Casper, J. H., "Permeable Surface Corrections for Ffowcs Williams and Hawkings Integrals," 11th AIAA/CEAS Aeroacoustics Conference, AIAA Paper No. 2005-2995, 2005.

[13] Redonnet, S., Manoha, E., and Sagaut, P., "Numerical Simulation of Propagation of Small Perturbations Interacting with Flows and Solid Bodies," Seventh AIAA/CEAS Aeroacoustics Conference, AIAA Paper No. 2001-222, 2001.

[14] Redonnet, S., Manoha, E., and Kenning, O., "Numerical Simulation of the Downstream Fan Noise of 3D Coaxial Engines," 11th AIAA/CEAS Aeroacoustics Conference, AIAA Paper No. 2005-2816, 2005.

[15] Redonnet, S., Desquesnes, G., and Manoha, E., "Numerical Study of Acoustic Installation Effects Through a Chimera CAA Method," 13th AIAA/CEAS Aeroacoustics Conference, AIAA No. 2007-3501, 2007.

[16] Gabard, G., Astley, R., and Tahar, M. B., "Noise Radiation from a Jet Pipe: A Benchmark Problem for Computational Aeroacoustics," 11th AIAA/CEAS Aeroacoustics Conference, AIAA Paper No. 2005-3064, 2005.

[17] Manera, J., Leneveu, R., Caro, S., and Mardjono, J., "Broadband Turbomachinery Noise: Exhaust Noise Computations with Actran/TM and Actran/DGM," AIAA Paper 2009-3292, 2009.

[18] Leneveu, R., Schiltz, B., Laldjee, S., and Caro, S., "Performance of a DGM Scheme for LEE and Applications to Aircraft Engine Exhaust Noise," AIAA Paper 2008-2884, 2008.

[19] Salem-Said, A.-H., and Ragab, S. A., "Large Eddy Simulation of the Interaction of Homogeneous Turbulence with a Flat-Plate Cascade," 12th AIAA/CEAS Aeroacoustics Conference, AIAA Paper No. 2006-1100, 2006.

[20] Lafronza, L., McAlpine, A., Keane, A. J., and Astley, R. J., "Response Surface Method Optimization of Uniform and Axially Segmented Duct Acoustics Liners," *Journal of Aircraft*, Vol. 43, No. 4, 2006, pp. 1089–1102. doi:10.2514/1.17727

[21] Polacsek, C., Desquesnes, G., and Reboul, G., "An Equivalent-Source Model for Simulating Noise Generation in Turbofan Engines," *Journal of Sound and Vibration*, Vol. 323, Nos. 3–5, 2009, pp. 697–717. doi:10.1016/j.jsv.2009.01.010

[22] Desquesnes, G., "Euler Equations in Perturbation 2.5-D: A New System for Acoustic Modal Propagation," 14th AIAA/CEAS Aeroacoustics Conference, AIAA Paper 2008-2822, 2008.

[23] Casalino, D., and Genito, M., "Achievements in the Numerical Modeling of Fan Noise Radiation From Aero-Engines," *Aerospace Science and Technology*, Vol. 12, No. 1, 2008, pp. 105–113. doi:10.1016/j.ast.2007.10.005

[24] Kok, J. C., "Computation of Sound Radiation from Cylindrical Ducts with Jets Using a High-Order Finite-Volume Method," 13th AIAA/CEAS Aeroacoustics Conference, AIAA Paper No. 2007- 3489, 2007.

[25] Michalke, A., "On Spatially Growing Disturbances in an Inviscid Shear Layer," *Journal of Fluid Mechanics*, Vol. 23, No. 3, 1965, pp. 521–544. doi:10.1017/S0022112065001520

[26] Bailly, C., and Juvé, D., "Numerical Solution of Acoustic Propagation Problems Using Linearized Euler Equations," *AIAA Journal*, Vol. 38, No. 1, 2000, pp. 22–29. doi:10.2514/2.949

[27] Huet, M., Fayard, B., Rahier, G., and Vuillot, F., "Numerical Investigation of the Micro-Jets Efficiency for Jet Noise Reduction," AIAA Paper 2009-3127, 2009.

[28] Redonnet, S., Mincu, C., and Manoha, E., "Computational Aeroacoustics of Realistic Co-Axial Engines," AIAA Paper 2008-2826, 2008.

[29] Tam, C., "Computational Aeroacoustics: Issues and Methods," *AIAA Journal*, Vol. 33, No. 10, 1995, pp. 1788–1796. doi:10.2514/3.12728

J. Astley
*Associate Editor*